Gravity Data Inversion by Adiabatic Quantum Computing

Giuliana Siddi Moreau,* Lorenzo Pisani, Andrea Mameli, Carlo Podda, Giacomo Cao, and Enrico Prati

A quantum-enhanced implementation of the binary inversion method for gravity data acquisition is discussed. The subsurface structure of a single density anomaly with an assigned density contrast is calculated by using a D-Wave adiabatic quantum computer. In particular, an iterative heuristic based on quantum annealing that recovers a sharp shape of the subsurface anomaly is developed. Such a task is accomplished by collecting partial images obtained by quantum annealing processes for optimal Lagrange penalty coefficients. The results are compared with those obtained according to the same cost function minimized via genetic algorithms by conventional hardware on a realistic 2D dataset. The outcomes of this work are promising as the reconstructed model is obtained in tenths of iterations instead of the hundreds required in conventional methods. Moreover, for the part of the computation that resides in the quantum processing unit, the computational cost of the single quantum annealing descent is constant with respect to the number of degrees of freedom of the subsurface grid. The implemented method is likely to reveal its full potential on forthcoming quantum annealing devices, outperforming existing techniques.

1. Introduction

The gravity geophysical method is used to map the subsurface density distributions starting from acquired measurements at the ground surface. The goal of inverse theory is to determine subsoil model parameters from real scale observations. Although a solution that satisfies the observed data can be easily found, its non-uniqueness is caused by the fact that, since gravity data are known only at the earth's surface, inversion is an ill posed problem in the sense of Hadamard, as it admits more than one solution.[1,2] Moreover, the method suffers from the under-determination of the problem, as there exist an infinite number of subsoil density distributions whose gravity response fits the acquired data in a least-squares sense.[3] To restrain the space of candidate solutions, the mathematical problem is represented by minimizing an objective function that contains a selection of suitable constraints.

In many cases the computational cost of available inversion techniques makes the inversion impractical for real models, as local minimization techniques, such as gradient descent, are not optimal for non-convex objective functions, and global optimization algorithms require a huge number of iterations to reach an acceptable solution.[3,4] While numerous works have been done on the subject, there are still many challenges remaining, including scaling up to large-scale problems and dealing with non-convexity.[5]

In recent years, adiabatic quantum computation has generated much interest for its potential to solve certain optimization problems that are difficult for classical computers,[6,7] in particular providing solutions for non-convex problems.[8] Thus, its application might be beneficial for solving a class of problems that exhibit cost functions featuring many local minima. Adiabatic quantum computers leverage the adiabatic theorem to perform minimization of the cost function.[9] They have been applied to several problems ranging from industrial applications such as logistics[10] and finance,[11] to quantum machine learning such as quantum restricted Boltzmann machines,[12,13] based on their capability to address quadratic unconstrained binary optimization (QUBO) problems.

In this work, we start with the binary formulation of Krahenbuhl and Li[4] that harnesses the linearity of density inversion and allows us to code density contrast values in the problem. One of the main advantages of this approach is that the solution exhibits a sharp boundary for the density anomaly in a computational framework that is characterized by the flexibility of density inversions. In exchange, the computational complexity increases as a minimization problem with binary constraints needs to be solved.

G. Siddi Moreau, L. Pisani, A. Mameli, C. Podda, G. Cao
CRS4
Loc. Piscina Manna Ed 1, Pula I-09050, Italy
E-mail: julie@crs4.it
G. Cao
Dipartimento di Ingegneria Meccanica Chimica e dei Materiali
Università degli Studi di Cagliari
Via Marengo 2, Cagliari I-09123, Italy
E. Prati
Istituto di Fotonica e Nanotecnologie
Consiglio Nazionale delle Ricerche
Piazza Leonardo da Vinci 32, Milano I-20133, Italy
E. Prati
Dipartimento di Fisica Aldo Pontremoli
Università degli Studi di Milano
Via Celoria 2, Milano I-20133, Italy

The difficulty of porting such a binary formulation on an adiabatic quantum computer lies in the fact that the resulting quadratic, unconstrained binary formulation gives rise to a complete graph with quadratic terms that vary in a range of different orders of magnitude. Because of the sparsity of the connections between the physical qubits, embedding techniques are required to supply highly connected virtual qubits. As embedding strategies on the Chimera and Pegasus layouts of current D-Wave hardware do not accomplish to find a perfect embedding to represent the original complete graph, our goal is to design a robust iterative algorithm that can exploit the performances of an adiabatic quantum computer to obtain good solutions to optimization problems. We then show the results obtained for a synthetic test case of a realistic 2D gravity problem with finite strike length, denoted as a 2.5D problem in the following sections. To build the numerical benchmarks, we use the same cross-section through the SEG/EAGE 3D salt model[14] considered previously by Krahenbuhl and Li.[4]

The results we obtain provide a good sharp subsurface model from surface data, whose quality is comparable to the reference work.[4] Despite limitations arising from mapping a complete problem graph on currently available quantum hardware do not allow it to neatly outperform classical results, the proposed heuristics reconstructs the subsurface model in less than ten macro-iterations, compared to the hundreds of generations required by genetic algorithms in the reference work.[4] Moreover, the hybrid quantum solution we provide for non-convex benchmarks in the presence of annihilators seems promising with respect to conventional solvers such as simulated annealing[15] and hybrid default D-Wave workflows. Moreover, the computational cost of the single quantum annealing descent in the quantum processing unit is constant with respect to the number of degrees of freedom of the subsurface model. In perspective, we expect that such implementations on the new generation of quantum annealing devices would outperform existing techniques, making the inversion usable for real models.

In Section 2, the inversion method proposed by Krakenbuhl and Li[4] is introduced and the inversion heuristics leveraging D-Wave quantum annealer is described. Section 3 gathers the results obtained for gravity data inversion of 2D realistic models with constant and variable density contrasts, while in Section 4, the results are discussed. Finally, Section 5 summarizes the main conclusions and the perspectives.

2. Method

2.1. Problem Statement

The inverse problem aims at recovering the unknown underlying parameters of a physical system that produce the available observations/measurements. The inversion method proposed by Krahenbuhl and Li[4] stems from Tikhonov regularization[16] and follows the data fitting approach that, as outlined in ref. [5], is based on four elements: the parametric model representation of the physics of the problem, the forward solver that evaluates a synthetic observation once the model parameters have been set, the objective function that expresses the misfit between synthetic observation and real data acquisition, and an optimization algorithm that evaluates the optimal model, that is, finds the set of model parameters that minimizes the misfit between synthetic and observed data. Usually, the above data fitting approach requires an iterative process where the forward problem is solved at each step.

In gravity data inversion, we consider the gravity anomaly at the Earth's surface as the observation for the inverse problem. The gravity anomaly is defined as the difference between the observed value of gravity acceleration along the vertical and the value predicted by a theoretical model that provides corrections from the effects of the nearby terrain, altitude, tidal effects, and so on. Some definitions of gravity anomalies can be found in ref. [17]. The gravity anomaly can reveal the presence of subsurface structures of unusual density.

Given a spatially varying density distribution $\rho^{(tot)}(x, y, z)$ in a domain V, the total gravity field $\boldsymbol{g}^{(tot)}$ is a three-component vector

$$\boldsymbol{g}^{(tot)} = \begin{bmatrix} g_x^{(tot)} \\ g_y^{(tot)} \\ g_z^{(tot)} \end{bmatrix} \tag{1}$$

described by the following equations:

$$\nabla \cdot \boldsymbol{g}^{(tot)} = -4\pi\gamma\rho^{(tot)} \tag{2}$$

$$\nabla \times \boldsymbol{g}^{(tot)} = 0 \tag{3}$$

where γ is the gravitational constant. Remark that solving the above system of equations is equivalent to state that the gravitational potential $u^{(tot)}(x, y, z)$ satisfies in the following Poisson's equation inside the domain V

$$\Delta u^{(tot)}(x, y, z) = -4\pi\gamma\rho^{(tot)}(x, y, z) \tag{4}$$

where Δ stands for the Laplace operator and the gravity vector $\boldsymbol{g}^{(tot)}$ is defined as the gradient of the gravitational potential $u^{(tot)}$

$$\boldsymbol{g}^{(tot)} = \nabla u^{(tot)} \tag{5}$$

Linearity of the Laplacian can be used further to separate the gravity contribution caused by the density of the planet Earth, to the best of our knowledge, from unknown density variations on the subsoil, which are the goal of the present research. By defining a "density contrast" ρ as

$$\rho^{(tot)}(x, y, z) = \rho^{(bg)}(x, y, z) + \rho(x, y, z) \tag{6}$$

namely the difference between the real density $\rho^{(tot)}(x, y, z)$ and a presumed background density distribution $\rho^{(bg)}$.

Under an appropriate choice of both the background density field value $\rho^{bg}(x, y, z)$ and the theoretical reference model for the $\boldsymbol{g}^{(bg)}$ in Equation (7), the gravity can be written as the sum of the gravity calculated from the value predicted by a theoretical model $\boldsymbol{g}^{(bg)}$ and a gravity anomaly $\boldsymbol{g}$, as

$$\boldsymbol{g}^{(tot)} = \boldsymbol{g}^{(bg)} + \boldsymbol{g} \tag{7}$$

**ADVANCED
SCIENCE NEWS**

www.advancedsciencenews.com

**ADVANCED
QUANTUM
TECHNOLOGIES**

www.advquantumtech.com

where both $g^{(\mathrm{bg})}$ and g abide by the same mathematical laws as $g^{(\mathrm{tot})}$ in Equations (2) and (3), respectively, with density distribution $\rho^{(\mathrm{bg})}(x, y, z)$ and $\rho(x, y, z)$. The same substitution holds in Equation (4) if we consider the gravitational potential $u(x, y, z)$ corresponding to the gravity anomaly g and the density contrast $\rho(x, y, z)$. Remark that, by definition, ρ can take negative values.

As far as the direct problem is concerned, instead of solving the gravitational potential equation corresponding to Equation (4) in the domain with appropriate boundary conditions, we prefer to use the integral representation of the solution of the above differential equation in a 3D volume V, namely

$$u(x', y', z') = \gamma \int \int \int_V \frac{\rho(x, y, z)\mathrm{d}x\,\mathrm{d}y\,\mathrm{d}z}{\sqrt{(x - x')^2 + (y - y')^2 + (z - z')^2}} \qquad (8)$$

where the integral is computed on the whole reference volume V.

The main advantage of this representation is that an expression for the vertical component of the gravity anomaly g as a function of the density contrast distribution $\rho(x, y, z)$ can be written by taking the partial derivative along the z-axis of the above equation.

For decades, gravity data surveys have acquired the vertical component of the gravity field at different equally spaced locations on a portion of the Earth's surface in order to provide a gravity anomaly dataset d_i^{obs}, denoting with $i = [1 .. N]$ the index ranging over the N acquisition stations.

In our study, as in ref. [4], acquired data d_i^{obs} refer to the z-component of the gravity anomaly g defined in Equation (7). The goal of the inversion method is hence to predict the density contrast distribution ρ that produces the observed vertical component of the gravity anomaly d_i^{obs} measured at N equally spaced stations at the acquisition plane.

Following the compact gravity inversion formulation, as from ref. [2] the subsurface region V is discretized as a set of voxel elements on a spatial Cartesian grid.

We consider a single material of known density contrast ρ, which may depend on the position, as the origin of the gravity anomaly. The mathematical inversion problem assumes a discrete nature and could be formulated by using binary variables. In particular, we can write

$$\rho_j(x, y, z) = \rho(x, y, z)\,\tau_j \qquad (9)$$

with $\rho(x, y, z)$ denoting the known expression for the density contrast at a spatial point (x, y, z) and τ_j being the corresponding binary variable defined at each voxel that switches on and off this contribution.

The predicted gravity response at the acquisition stations d_i^{pred} can be described as a weighted sum of the contributions of the density contrast of voxel elements on a spatial Cartesian grid,

$$d_i^{\mathrm{pred}} = \sum_j \rho(x, y, z)\tau_j G_j^{(i)} \qquad (10)$$

where the weights $G_j^{(i)}$ are Green functions that come from the integration of Equation (8).

Among the choice of possible Green functions, we choose the simplest expression that corresponds to lumping the jth voxel mass at its barycenter, see ref. [18] for more details. For a 2D discretization of voxels in the xz-plane, denoting with x_i, z_i and x_j, z_j the horizontal and vertical coordinates of acquisition station i and the generic voxel j we have the simple expression

$$G_j^{(i)} = -2\,\pi a^2 \gamma \frac{(z_i - z_j)}{(x_i - x_j)^2 + (z_i - z_j)^2} \qquad (11)$$

where a is the radius of the lumped mass as an infinite cylinder in the y-direction.

We can state the objective function for the inversion problem as from ref. [2], which is a weighted sum of the model objective function Φ_{m} and data misfit Φ_{d}, which can be stated as follows:

Minimize Φ_{m}

subject to $\Phi_{\mathrm{d}} = 0$ and $\rho = \{0, \rho(x, y, z)\}$ \qquad (12)

where we have as well a suitable set of constraints on the binary value of voxels' sets of the subsurface discretization to insert all information arising from prior knowledge on the value of the density contrast.

In our study, the data misfit function is defined as

$$\Phi_{\mathrm{d}} = \sum_{i=1}^N \left(\frac{d_i^{\mathrm{obs}} - d_i^{\mathrm{pred}}}{\sigma_{\mathrm{d}}} \right)^2 \qquad (13)$$

where σ_{d} stands for the standard deviation of the observed distribution at the acquisition surface and d_i^{pred} terms are obtained as in Equation (10).

The model function Φ_{m} is a generic model objective function that accounts for the area of the model, favors compact solutions and can be defined as

$$\Phi_{\mathrm{m}} = \sum_j \tau_j^2 \qquad (14)$$

Differently from the work of Krahenbuhl and Li[4] we drop in Equation (14) the model function terms that control the flatness in different spatial directions. The source of this simplification relies on the empirical observation that on the adiabatic annealer we have not recorded any noticeable effect in maintaining these terms even for the extremely high values specified in the ref. [4].

In this way, our objective function can be written as

$$\Phi = \Phi_{\mathrm{m}} + \frac{1}{2}\lambda_{\mathrm{d}}^2 \Phi_{\mathrm{d}} \qquad (15)$$

where λ_{d} is an appropriate scalar used to enforce the constraint as a Lagrange penalty term. In this manner we are restraining the choice of the λ_{d} term to positive values.

The reason for this choice is that if we constrain the model objective function by means of a Lagrange penalty term, we are forced to perform grid search for hyper-parameter tuning. Simple grid search for the λ_{d} hyper-parameter in our case is not very effective as the density discontinuity expands its volume at increasing values of λ_{d}, but when the Lagrangian penalty

**ADVANCED
SCIENCE NEWS**

www.advancedsciencenews.com

**ADVANCED
QUANTUM
TECHNOLOGIES**

www.advquantumtech.com

coefficient is lower than the optimal value the adiabatic solver provides an empty solution where all binary variables are set to zero. The choice of an optimal value depends on the dataset and on the hardware beneath. The problem statement as in Equation (15) allows for an automated selection of the Lagrange penalty term via gradient descent.

We recast the objective function in order to bind the Lagrangian penalty term to the L2 residual between observed and modeled data over the acquisition points as reported in what follows,

$$\lambda_d^{new} = \lambda_d - \eta \frac{\partial \Phi}{\partial \lambda_d} \tag{16}$$

keeping into account that

$$\frac{\partial \Phi}{\partial \lambda_d} = \lambda_d \Phi_d + \frac{\lambda_d^2}{2} \nabla_\lambda \Phi_d \tag{17}$$

where the gradient of the L2 residual with respect to λ_d in Equation (17) is evaluated numerically with finite differences as follows

$$\nabla_\lambda \Phi_d = \frac{[\Phi_d]^{(cur)} - [\Phi_d]^{(prev)}}{\lambda_d^{(cur)} - \lambda_d^{(prev)}} \tag{18}$$

The parameter η in Equation (16) is a learning rate for the gradient descent. As in machine learning works, we set η to a constant value.

We have also tested in our numerical experiments an empirical update rule for the λ_d parameter that bonds its value to the L1 residual. Its application is valid only for constant density contrast as only in this case λ_d is a monotonic function of L1 norm. Our empirical relation is

$$\lambda_d^{new} = \lambda_d - \eta \lambda_d \sum_i \left(d_i^{(obs)} - d_i^{(pred)} \right) \tag{19}$$

and η is a constant learning rate.

2.2. Solution of the Optimization Problem on D-Wave Quantum Annealer

The solution to the inversion problem of the original work of Krahenburg and Li[4] was demanded to genetic algorithms, that belong to the metaheuristic class that applies to non-convex minimization problems. The quantum annealer approach is conceptually closer to another classic metaheuristic algorithm, standard simulated annealing.

Starting from the objective function obtained from Equations (13)–(15), we can recast the inversion problem in Equation (12) as a QUBO problem.

The D-Wave quantum processing unit (QPU) can be viewed as a heuristic that minimizes QUBO objective functions using a physically realized version of quantum annealing.[19]

A QUBO problem is defined using an upper-triangular matrix of real weights Q and a vector of binary variables τ as minimizing the function

$$f(\tau) = \sum_i Q_{i,i} \tau_i + \sum_{i<j} Q_{i,j} \tau_i \tau_j \tag{20}$$

where the diagonal terms $Q_{i,i}$ are the linear coefficients and the nonzero off-diagonal terms $Q_{i,j}$ are the quadratic coefficients.

In particular, while the model function Φ_m has a simple expression in terms of the square of the binary coefficients (see Equation (14)) and it is implemented as a linear term as the square of a binary variable is the binary variable itself, the data misfit function Φ_d can be expressed as

$$\Phi_d = \frac{1}{\sigma_d^2} \sum_i \left(\left(d_i^{(obs)} \right)^2 - 2 d_i^{(obs)} \sum_j \tau_j \rho_j G_j^{(i)} + \tau_j (\rho_j G_j^{(i)})^2 \right.$$
$$\left. + 2 \sum_j \sum_{l<j} \tau_j \tau_l \rho_j \rho_l G_j^{(i)} G_l^{(i)} \right) \tag{21}$$

The difficulty of porting such a binary formulation on an adiabatic quantum computer lies in the fact that the resulting quadratic unconstrained binary formulation gives rise to a complete graph, with quadratic terms that vary in a range of different orders of magnitude. The Green functions appearing in the last term of Equation (21) induce a full coupling of the degrees of freedom of the problem, where the value of linear and quadratic terms varies with depth.

Moreover, Leap's quantum-classical hybrid solver solutions are not guaranteed to be optimal.[20]

Ideally, if the quantum annealing devices were capable of mapping a QUBO raised from a complete graph having coefficients covering a wide range of magnitude orders, a single annealing descent process with an optimal Lagrange parameter would be sufficient to obtain the solution to our inversion problem.

Embedding algorithms[21,22] on the Chimera and Pegasus layouts of current D-Wave hardware are proven to get the objective function value close to the global minimum value. Even if they cannot yet provide a full representation of the original complete graph, the solution they evaluate is locally optimal.

The solution we obtain in a single annealing is affected by two issues.[20] First, each QPU has an allowed range of values for the biases and strengths of qubits and couplers. The values defined in the inversion problem are adjusted to fit the entire available range.[20] Green function contributions entering in the quadratic terms that do not fit in this range are cut off. So we have to redefine the binary quadratic model iteratively, working on the misfit of the residuals between the acquired data and the predicted response at the previous iteration, to be sure to account for all minor contributions. Second, at each annealing descent, a subset of the variables of the binary quadratic model are considered active in order to make the problem fit in the available quantum processor.

By keeping into account these issues, we adopt a divide-and-conquer strategy to obtain meaningful solutions for our problem, in which the number of active qubits in the QUBO is reduced, taking into account the response evaluated in previous

2300152 (4 of 13)

**ADVANCED
SCIENCE NEWS**

www.advancedsciencenews.com

**ADVANCED
QUANTUM
TECHNOLOGIES**

www.advquantumtech.com

steps. This strategy is feasible as gravity inversion is a linear problem in which superposition holds,[23] hence the response from composite structures is equal to the sum of responses from the individual structures, and there is no interaction among the partial structures.

The details of the algorithm will be given in the following pages.

Our concern is hence to design a heuristic that can exploit the performances of available quantum processing units to find quickly good solutions to optimization problems arising from inversion.

Inversion methods undergo the general principle that, in order to get a unique solution, the dimensionality of the data must match the dimensionality of the physical property one is trying to recover.[23] The uniqueness statement impacts upon how much information must be supplied by the user to obtain a geologically meaningful model for interpretation. For example, if theoretical uniqueness exists, then by acquiring sufficient data, and by imposing certain continuity conditions, such as requiring the model to be smooth to some extent, then inversion may be able to recover larger scale features of the earth. In our case, the gravity acquisition provided in ref. [4] is a set of measurements collected at 41 points equally distributed along the acquisition line, whose number does not provide sufficient information for a stable inversion. To increase the number of control points for the least-square minimization and improve the conditioning of the problem matrix, we interpolate the gravity acquisition on a finer grid of 481 points by means of univariate splines that have shown to be a good choice for noisy data.[24] For finer spatial discretizations the number of interpolated points for the gravity acquisition was increased keeping the ratio between number of interpolated points and total qubits to 0.35. Tukey windowing[25] of the acquisition is also performed before interpolation to avoid deep artifacts in the image induced by noisy values of first and last samples of the signal.

Finally, we have to identify a stopping criteria of the inversion process. For this goal, at each iteration of the partial image computation we evaluate the ratio of the L2 norm of the misfit between observed and modeled gravity data at the acquisition surface and the L2 norm of the observed data, that has to be less than a threshold ϵ specified by the user as follows

$$\frac{\sum_i (d_i^{\text{obs}} - d_i^{\text{pred}})^2}{\sum_i (d^{\text{obs}})^2} < \epsilon \qquad (22)$$

We provide herein a walk-through of the procedure we propose for the divide-and-conquer heuristics. The main stage, defined in Algorithm A1, consists of two nested loops: the "macro" loop that iterates to construct partial subsoil images whose sum will form the shape of the buried density anomaly and the "micro" loop whose micro-iterations are carried out to find the proper penalty value λ_d that allows to reconstruct the contributions to the current partial image in the outer "macro" loop. In this main stage, we carry out the following steps: i) at each macro-iteration we feed the inversion process with the observed data at iteration 0 and with the residual between observed data and predicted data at the previous steps for the next iterations; ii) we start performing the cycle of micro-iterations in order to find the optimal λ_d

Algorithm A1 Main stage of inversion heuristics.

Input: Observed gravity data d_i^{obs} at the N acquisition points. Matrix C_z of dimensions (nz, nx) contains the binary variables corresponding to spatial voxels set to zero as the constraints of Equation (12) (namely the zero constraint map as in the bottom panel of Figure 1); ϵ threshold value provided by the user for the L2 ratio stopping criterium in Equation (22); N_{iter} stands for maximum number of iterations to be performed in this stage (default: 8).

Output: Matrix I_f of dimensions (nz, nx) contains the binary variables corresponding to spatial voxels of the subsoil model; list of matrices LI_p contains the partial images for each annealing descent with optimal λ_d.

Functions: *eval_pred*: given an image I of dimensions (nz, nx) that contains the binary variables corresponding to the partial solution, it evaluates the predicted gravity response using Equation (10); *eval_part_image*: given an active set of zero constraints C_z and the $d_i^{\text{obs}} - d_i^{\text{pred}}$ evaluates the corresponding binary quadratic model as in Equation (15) and via gradient iteration finds the partial optimal value λ_d; *eval_L2_ratio* computes the L2 ratio in Equation (22) from the original acquisition d_i^{obs} and from d_i^{pred} response of the current I_f image. The matrix O stands for an image of the same dimensions of I_p having all zero entries.

```
1:   I_f ← O
2:   C_z^(cur) ← C_z
3:   d_i^(res) ← d_i^(obs)
4:   Li_p ← empty list
5:   for m = 0, N_iter do
6:       I_p = eval_part_image(C_z^(cur), d_i^(res))
7:       d_i^(pred,p) = eval_pred(I_p)
8:       LI_p.append(I_p)
9:       I_f ← I_f + I_p
10:      d_i^(res) ← d_i^(res) − d_i^(pred,p)
11:      C_z^(cur) ← C_z^(cur) + I_p
12:      d_i^(pred) ← d_i^(pred) + d_i^(pred,p)
13:      ε^(cur) = eval_L2_ratio(d_i^(obs), d_i^(pred))
14:      if ε^(cur) < ε then
15:          exit
16:      end if
17:  end for
```

penalty value that minimizes the misfit and get the partial response I_p (this is done by carrying out annealer descents in line 6 of Algorithm A1 for different λ_d values inside the block labeled *eval_part_image*; iii) we evaluate the predicted gravity response for the partial image I_p in line 7; iv) we freeze the one-valued binary variables that belong to the partial response I_p for the next iteration in line 11; v) we accumulate partial structures in the first image I_f of the anomaly, in addiction single partial images I_p of different macro-iterations of the first stage are stored in the list L_i to map contributions of different iterations. The inner micro-iteration loop on the residual terminates when the solver finds empty solutions for all λ_d values. The outer macro-iteration loop has an early exit condition that the L2 ratio value (Equation (22), line 13) drops below the input threshold ϵ (line 14). The final image of the anomaly will gather the partial responses we have obtained through this stage of macro-iterations.

In this study we mainly employ a standard sampler together with a cutoff composer applied on an autoembedded one, setting
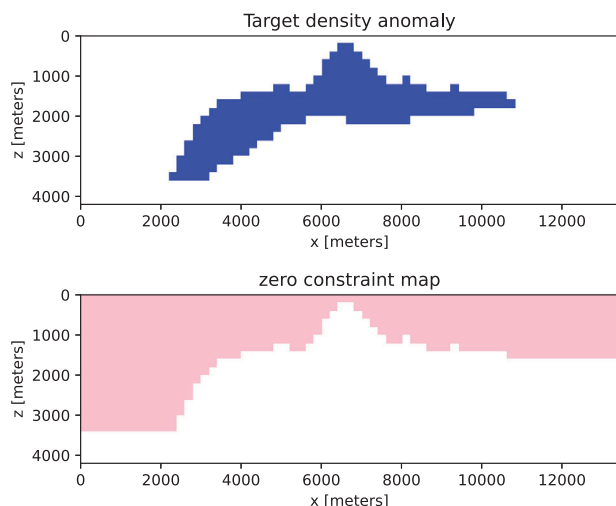
Figure 1. The 2.5D density contrast model is displayed in the top panel. The cross-section, drawn from the converted SEG/EAGE salt model, has a density contrast of -0.2 g cm^{-3}. At the bottom, a plot of the constrained region for the model is displayed. The pink-colored area highlights the binary variables set to zero.

the threshold to 0.75 over 1000 shots. Kerberos and Hybrid hybrid workflows[26] were also used to compare the response.

Moreover, our aim is to design an inversion process whose results are minimally affected by the topology of the embedding or by different outcomes of the annealing process, provided that we cannot obtain a solution that is bitwise the same due to the probabilistic nature of the quantum computation. For this aim, as the cutoff composer may produce discontinuities in the solution due to chain breaks, sometimes we had to perform local optimization on the annealer result using the steepest descent solver as postprocessing.

3. Results

3.1. 2D Gravity Problem with a Constant Density Contrast

As a first application of the binary inversion of gravity data, we build the same 2.5D test case as,[4] involving a salt body of constant density contrast. This constant density contrast use-case will be referred to as benchmark 3.1 in the following sections.

We consider the same 2D section utilized in the work of ref. [4] drawn from the SEG/EAGE salt model,[14] designed as a realistic synthetic dataset to provide a benchmark for the geophysical community.

In the same way, as in the reference work, the geometrical structure of the salt body is maintained to build a 2D model featuring a uniform density contrast to feed the binary inversion process.

For the 2.5D problem, the salt body cross-section displayed in **Figure 1** is used to construct a model characterized by a uniform density contrast of -0.2 g cm^{-3}. This salt shape is embedded in a uniform half-space. The acquisition layout consists of a finite strike length of 20 km in and out of the page.

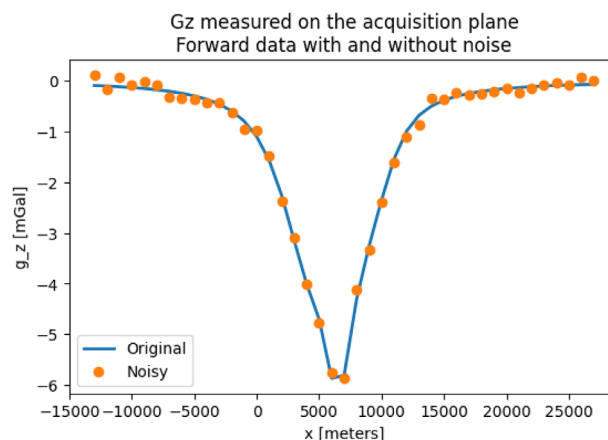As in the reference work,[4] synthetic gravity data are calculated via a 2.5D direct gravity problem.

Figure 2. Synthetic acquisition generated for 2.5D density contrast model from the converted SEG/EAGE salt model: analytic data (line) and noise-contaminated data (points). Gaussian white noise has a zero mean and a standard deviation of 0.1 mGal.

In order to simulate observed gravity data, we contaminate the synthetic gravity data obtained from the above model with uncorrelated Gaussian noise with a zero mean and a standard deviation of 0.1 mGal (see **Figure 2**).

To simulate a realistic application of the algorithm and to restrain the space of unrealistic solutions, we incorporate the information of the known top of salt into each model through a zero constraint imposed at each corresponding binary variable occurring in the above area, that appears colored in pink in Figure 1 in the bottom panel. The salt top geometry is usually easily available from some other standard geophysical processing, such as seismic imaging. The adoption of the constraint raising from the position of the top of the salt and white noise contamination was utilized in the reference work.[4] As pointed out in the seminal work of Li and Oldenburg,[2] an inversion process that minimizes the data misfit at the surface will generate a density distribution that is concentrated near the surface. Imposing the upper profile of the salt top via the zero constraint binary map filters out the non-physical solutions that feature this unwanted behavior.

The computational model for the binary inversion consists of a rectangular domain whose depth ranges from the surface to 4200 m, and the horizontal dimension spans from 0 to 13 400 m. We adopted three different subsurface discretizations to assess the scalability of the method. As we can see in **Table 1** in the coarser discretization, denoted with A, the model region is divided into 1407 rectangular cells (67×21). In the intermediate one, labeled

Table 1. Set of three different spatial discretizations used to assess the scalability of the method. The first column shows the mesh label, the second one displays the number of points of the spatial discretization along the x- and z-axis, the third column and the fourth column gather the total number of qubits and the number of active qubits after the imposition of the constraint that sets binary values to zero.

Label	Spatial discretization	Total qubits	Active qubits
A	67×21	1407	825
B	89×28	2492	1420
C	133×42	5586	3232

2300152 (6 of 13)

**ADVANCED
SCIENCE NEWS**

www.advancedsciencenews.com

**ADVANCED
QUANTUM
TECHNOLOGIES**

www.advquantumtech.com

as B, the model region is divided into 2492 rectangular cells (89×28). In the finer one, labeled as C, the model region is discretized into 5586 rectangular cells (133×42). For each computational grid every cell is associated to a different qubit, summing up to a total number of qubits displayed in Table 1. The last column of Table 1 displays the number of active qubits, that is, the effective variables in the problem solution after the imposition of the zero constraint binary map. We use the model objective function shown in Equation (15).

As we illustrated in the previous section, in the iterative process of the main stage we compute partial solutions and we iterate evaluating the misfit between the acquired and modeled data at the nth step to evaluate the next partial image. Binary variables that are set to one in the previous partial images are frozen for the evaluation of the current binary quadratic models. The test was run on three different QPUs, D-Wave Advantage2 prototype 1.1, Advantage 4.1 and on DW2000v6, getting the same results from a qualitative point of view. The threshold for convergence of the L2 norm ratio was set to 0.005. We used the Lagrange parameter to update the definition based on the L1 norm in Equation (19). The numerical setup of the inversion process involves up to 12 micro-iterations allowed to find the optimal Lagrange penalty value by means of gradient descent into the same macro-iteration.

In all benchmarks the fundamental contributions to the image were provided in the first three macro-iterations providing solutions that were below the relative L2 error threshold of 0.02, hence if we set this value as error threshold we get a satisfactory image that is really close to the final one after three macro-iterations. In the main stage, the first six quadratic models happen to have a valid value of λ_d and a seventh macro-iteration on residual with empty results terminates the main stage.

The final results for the set of discretizations described above are displayed in the three top panels of **Figure 3** in blue. **Figure 4** shows predicted (solid line) and observed (dotted line) gravity acquisitions at the end of the inversion loop for the coarser discretization (A) in Table 1. **Figure 5** shows the relative L2 residual drop across seven macro-iterations for the set of three numerical discretizations described in Table 1.

Finally, for the same final results displayed in Figure 3, an overlay of the real shape of target is superposed in orange in **Figure 6**. Matching voxels between target and imaged density discontinuities appear colored purple. The convergence threshold is low, but as the inversion problem is ill posed we might have identified a solution that produces the same gravity imprint within the given tolerance expressed by the L2 ratio.

As it can be noticed in Figure 6 the quality of the recovered image needs further work to be improved, mainly due to the attenuation of the Green function weights that were not magnified.

To assess that the accuracy issue was not induced by the quantum computation, we ran the same benchmarks to solve the same quadratic unconstrained binary optimization problem by means of the conventional simulated annealing (SA)[27] implemented in D-Wave software suite following the original approach by Kirkpatrick.[15] As far as local minima determination is concerned, the interested reader is referred to the work of Koshka[28] for a characterization of the differences between the solutions obtained via quantum annealing and conventional simulated annealing. In **Figure 7**, the results of the same benchmarks for conventional simulated annealing are presented. In this con-
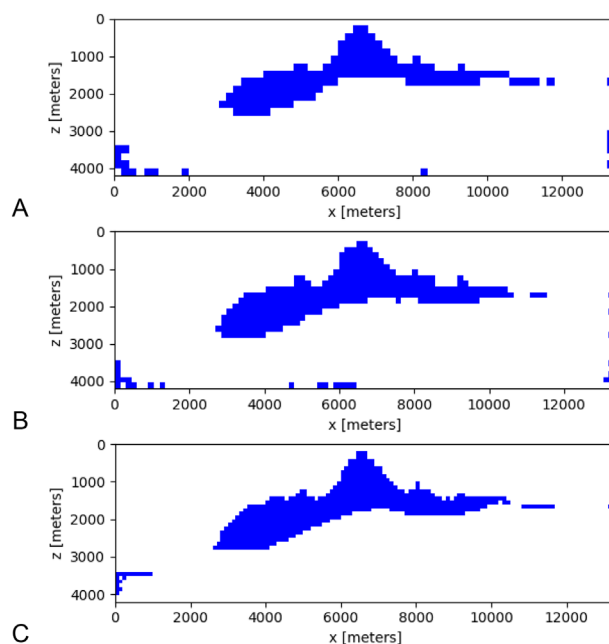

Figure 3. Inversion results obtained on the realistic acquisition contaminated by uncorrelated Gaussian noise for 41 stations along the 40-km survey line, run on D-Wave Advantage 5.1. For the update of the Lagrange parameter we adopt the L1 ratio. The three panels display the final result of the inversion process over the three computational grids A, B, and C described in Table 1.

stant background density contrast use case, the results obtained via conventional simulated annealing are equivalent to those obtained by a quantum annealer over the three discretizations 6, as far as the shape of the recovery anomaly is concerned.

A second numerical experiment was run on D-Wave Advantage 5.1 changing the update rule of the Lagrange value in the
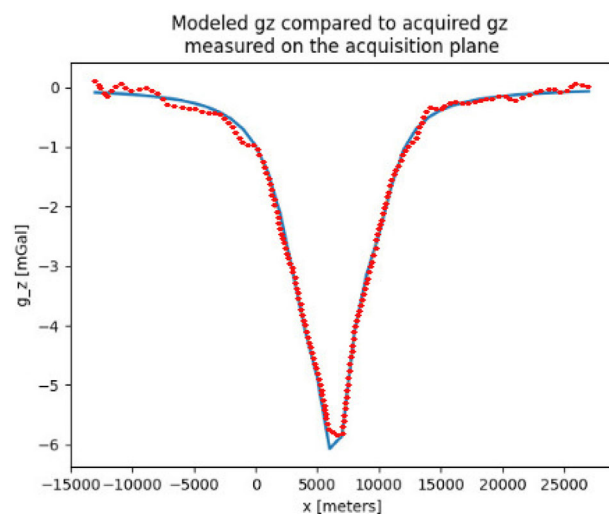

Figure 4. Inversion results obtained on the realistic acquisition contaminated by uncorrelated Gaussian noise for 41 stations along the 40-km survey line, run on D-Wave Advantage 5.1. For the update of the Lagrange parameter we adopt the L1 ratio.Predicted and observed gravity acquisitions for benchmark A, respectively plotted with solid line and dotted line.
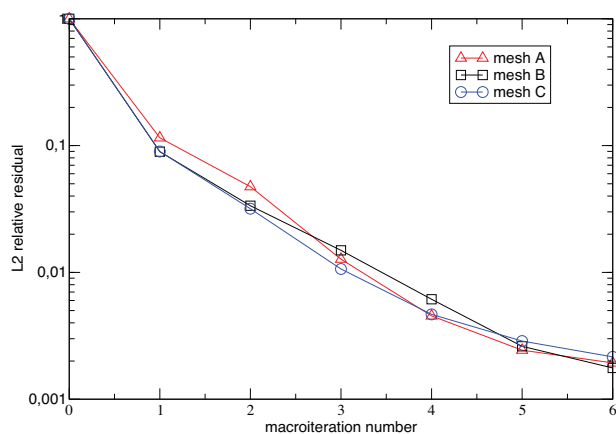
**ADVANCED
SCIENCE NEWS**

www.advancedsciencenews.com

**ADVANCED
QUANTUM
TECHNOLOGIES**

www.advquantumtech.com

Figure 5. Inversion results obtained on the realistic acquisition contaminated by uncorrelated Gaussian noise for 41 stations along the 40-km survey line, run on D-Wave Advantage 5.1. The graph displays the L2 residual ratio drop across macro-iterations for the set of three discretizations described in Table 1.

inner optimization loop. In this numerical simulation, we used the empirical update of the Lagrange parameter in Equation (16). The threshold for convergence of the L2 norm ratio was set to 0.005. The numerical setup of the inversion process involves up to 12 iterations allowed to find the optimal Lagrange penalty value by means of gradient descent into the same macro iteration; in
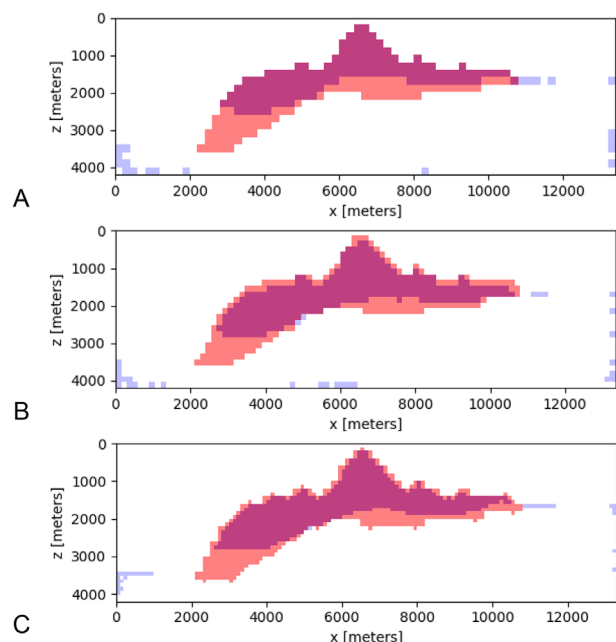

Figure 6. Inversion results obtained on the realistic acquisition contaminated by uncorrelated Gaussian noise for 41 stations along the 40-km survey line, run on D-Wave Advantage 5.1. For the update of the Lagrange parameter we adopt the L1 based definition. The three panels display the final result of the inversion process over the three computational grids (A, B, C described in Table 1, from top to bottom), colored in blue, the real shape of the target is overlaid in orange. Matching voxels are highlighted in purple.
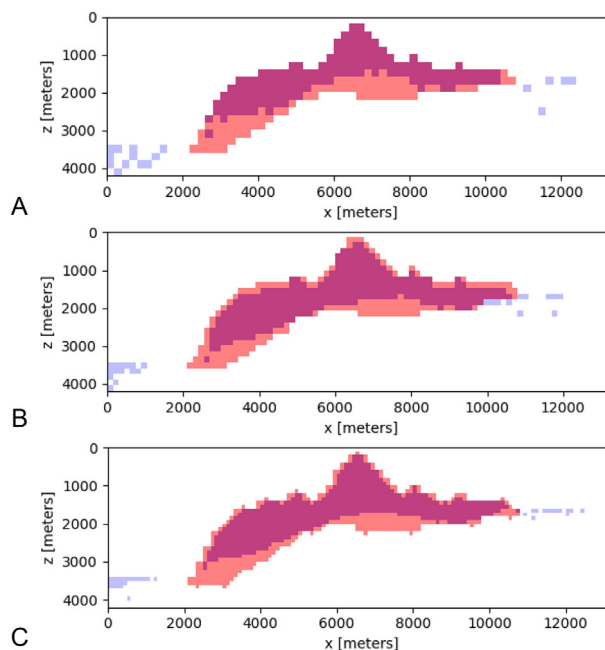

Figure 7. Inversion results obtained on the realistic acquisition contaminated by uncorrelated Gaussian noise for 41 stations along the 40-km survey line, run on a conventional high performance computing node by means of simulated annealing. For the update of the Lagrange parameter we adopt the L1 based definition. The three panels display the final result of the inversion process over the three computational grids (A, B, C described in Table 1, from top to bottom), colored in blue, the real shape of the target is overlaid in orange. Matching voxels are highlighted in purple.

the main stage, we count seven macro-iterations. The final results of the model for each one of the three discretizations are displayed in **Figure 8** in blue, and an overlay of the real shape of the target is superposed in pink. Matching voxels between target and imaged density discontinuities appear colored in purple. In Figure 8, the final results of the run on discretizations A, B, and C are presented. As it might be seen, for this constant background density contrast use case, the shape of the recovered anomaly is practically the same as in Figure 6.

As the way of implementing the algorithm makes use of standard D-Wave workflows without customizing the embedding, we get the same results on the DW2000v6 Quantum Processor.

3.2. 2D Gravity Problem with a Variable Density Contrast

As in the work of ref. [4], in this test case we inspect the performances of our implementation on a more realistic model that features density contrast reversal to mimic the presence of an annihilator that is, a nonzero density distribution that produces no external field for a particular source geometry.[29] The annihilator quantitatively describes the nonuniqueness of potential field data because any amount of the annihilator can be added to a possible solution without affecting the field of the source, therefore, the corresponding optimization function is non-convex.

In the presence of an annihilator, gravity data contributions arising from the upper and lower portions of the anomaly have opposite signs. In the surface gravity data acquisition, a portion
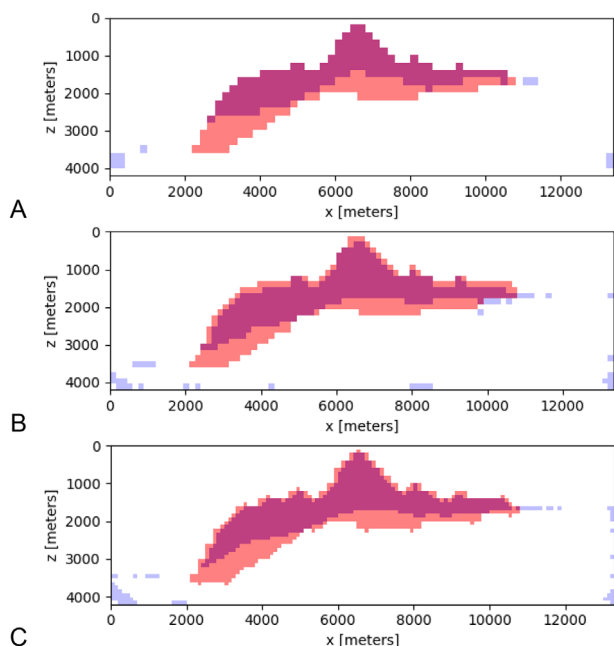
**ADVANCED
SCIENCE NEWS**

www.advancedsciencenews.com

**ADVANCED
QUANTUM
TECHNOLOGIES**

www.advquantumtech.com

A

B

C

Figure 8. Inversion results obtained on the realistic acquisition contaminated by uncorrelated Gaussian noise for 41 stations along the 40-km survey line, run on D-Wave Advantage 5.1. For the set of discretizations A, B, and C the panels display the final result of the inversion process, colored in blue, The real shape of the target is overlaid in orange. Matching voxels are highlighted in purple. These results were obtained with the update formula for the Lagrange parameter in Equation (16).

Figure 9. On the top the 2.5D density contrast model is displayed The geometry is drawn from the converted SEG/EAGE salt model, Above 1800 m the salt body has a density contrast value of +0.2 g cm^{-3} (displayed in green), whereas below that depth salt density contrast is −0.2 g cm^{-3} (colored in blue). At the bottom a plot of the constrained region for the model is displayed. The pink colored area highlights the binary variables set to zero.

of the signal is zero: this is a challenging condition for numerical implementations of continuous variable gravity inversion methods.

This variable density contrast use-case will be referred to as benchmark 3.2 in the following sections.

Following the work of ref. [4], we modify the same 2D section as in the previous test case in order to provide the density contrast reversal displayed in **Figure 9**. The rectangular model domain has the same extension, spanning from 0 to 4200 m in depth and from 0 to 13 400 m along the horizontal dimension. The same discretization is kept as well, resulting in a grid of 1407 rectangular cells (67 × 21). The salt body density contrast value is set to of +0.2 g cm^{-3} above the depth of 1800 m, and is −0.2 g cm^{-3} below that depth.

As far as the synthetic gravity data acquisition is concerned, we provide the same layout as in Section 3.1, setting 41 stations along a 40-km survey line. Observed data are generated by adding uncorrelated Gaussian noise with a zero mean and a standard deviation of 0.1 mGal to the synthetic data calculated at the 41 stations, **Figure 10**. The above observed data clearly display the effect of density contrast reversal, as the gravity anomaly varies between −1 and +2 mGal.

As far as the numerical setup was concerned, the threshold for the convergence of the L2 norm ratio was set to 0.05. The inner loop for the search of the optimal λ_d in 17 was composed of 25 iterations. The benchmark was conducted over discretizations A and B. Remark that the solution found at first macro-iteration is obtained via cutoff embedding without any postprocessing, as for non-convex cases greedy solver postprocessing worsens the
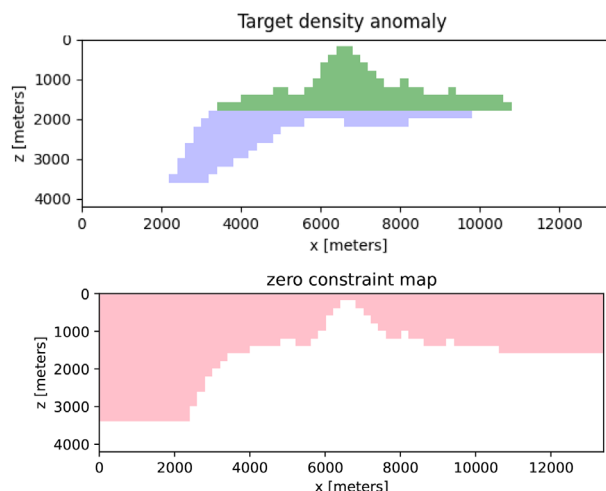
solution. As the run on the quantum annealer performed only one macro-iteration and exited without finding any valid solution at the second macro-iteration, we decided to carry out a hybrid approach and solve the second macro-iteration with conventional simulated annealing. Hence, a total amount of two macro-iterations for partial results computation is performed.

As we can see in **Figures 11** and **12**, further work is needed to provide an accurate result for the varying velocity contrast in the presence of nil zones. Apparently, the quantum solution recovers a coarse global shape in the presence of nil zones, and one single macro-iteration of conventional simulated annealing improves the solution. This benchmark is particularly tough as
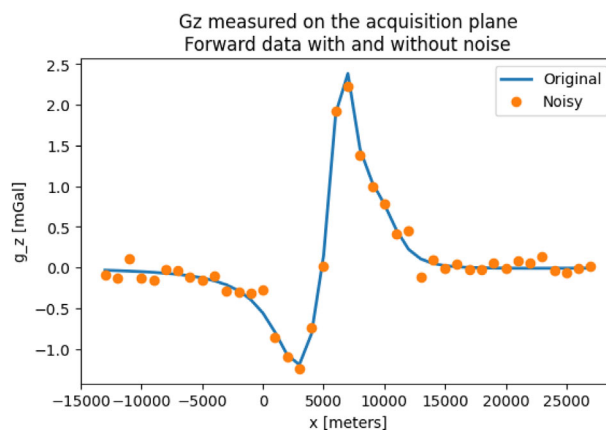

Figure 10. Synthetic acquisition generated for 2.5D density contrast model with nil zone from the converted SEG/EAGE salt model: Analytic data (line) and noise-contaminated data (points). Gaussian white noise has zero mean and standard deviation of 0.1 mGal. The effect of density contrast reversal is apparent in the data with an anomaly varying between −1 and +2 mGal.

**ADVANCED
SCIENCE NEWS**

www.advancedsciencenews.com

**ADVANCED
QUANTUM
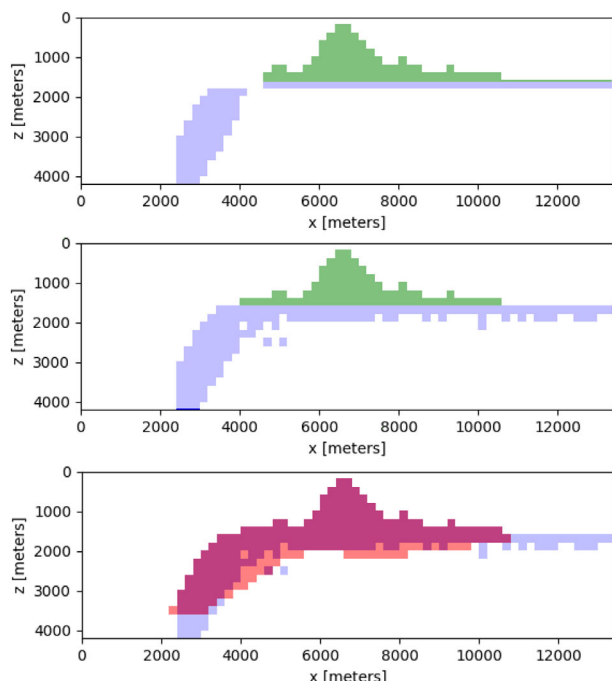TECHNOLOGIES**

www.advquantumtech.com

Figure 11. Inversion results obtained on the realistic acquisition contaminated by uncorrelated Gaussian noise for 41 stations along the 40-km survey line, run on D-Wave Advantage 4.1. over discretization A. The result of the first macro-iteration of quantum annealing with optimal lambda value is shown in the top panel. In the above panels the resulting shape is colored with the corresponding density contrast: Above 1800 m the value is $+0.2$ g cm^{-3} (displayed in green), whereas below that depth the salt density contrast is -0.2 g cm^{-3} (colored in blue). Then another macro iteration is performed using conventional simulated annealing with optimal lambda value, whose result is shown in the second panel from top. The third panel from top displays the final result of the inversion process, colored in blue. The real shape of the target is overlaid in orange. Matching voxels are highlighted in purple.
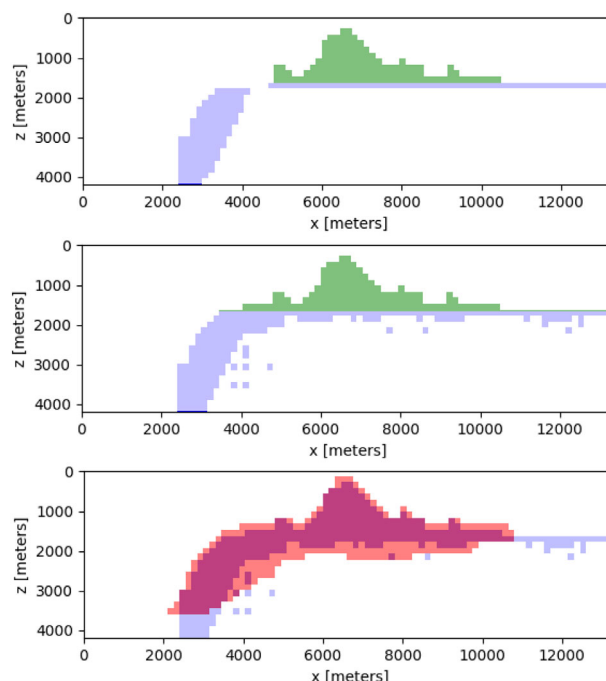

Figure 12. Inversion results obtained on the realistic acquisition contaminated by uncorrelated Gaussian noise for 41 stations along the 40-km survey line, run on D-Wave Advantage 4.1. over discretization B. The result of the first macro-iteration of quantum annealing with optimal lambda value is shown in the top panel. In the above panels the resulting shape is colored with the corresponding density contrast: Above 1800 m the value is $+0.2$ g cm^{-3} (displayed in green), whereas below that depth the salt density contrast is -0.2 g cm^{-3} (colored in blue). Then another macro iteration is performed using conventional simulated annealing with optimal lambda value, whose result is shown in the second panel from top. The third panel from top displays the final result of the inversion process, colored in blue. The real shape of the target is overlaid in orange. Matching voxels are highlighted in purple.

the non-convexity of the cost function leads many solvers to solutions that are local minima of the cost functions. Conventional methods such as simulated annealing, used to solve the same quadratic unconstrained binary problem with the same heuristics, provide a qualitatively worse solution, as in **Figure 13**. D-Wave hybrid workflows such as Kerberos provide a worse solution as well, as shown in **Figure 14**.

However, the proposed heuristic manages to build a solution even in this difficult case, and the results presented for the same numerical setup in the ref. [4] reflect this trouble.

4. Discussion

Despite the limitations arising when mapping a complete problem graph on existing quantum hardware do not allow to neatly outperform classical results in the convex optimization case in benchmark 3.1, the proposed heuristics make the constrained gravity data inversion a usable technique that reconstructs the subsurface model in less than 10 macro-iterations, compared to the hundreds of generations required by genetic algorithms in the ref. [4]. Moreover, the hybrid quantum solution we provide for the non-convex benchmark 3.2 in the presence of annihilators
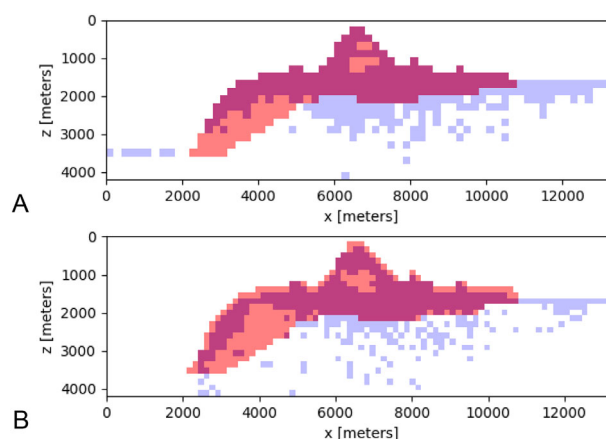

Figure 13. Inversion results obtained on the realistic acquisition contaminated by uncorrelated Gaussian noise for 41 stations along the 40-km survey line, run a conventional high performance computing node over discretizations A and B. The results of seven macro-iterations of conventional simulated annealing (SA) with optimal lambda value are shown for discretizations A and B, colored in blue, The real shape of the target is overlaid in orange. Matching voxels are highlighted in purple.

**ADVANCED
SCIENCE NEWS**

www.advancedsciencenews.com

**ADVANCED
QUANTUM
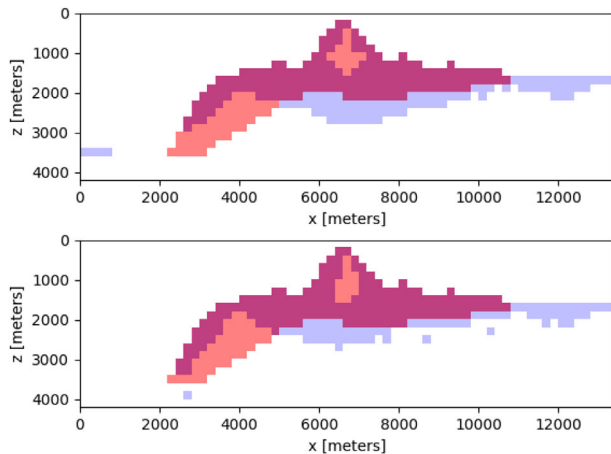TECHNOLOGIES**

www.advquantumtech.com

Figure 14. Inversion results obtained on the realistic acquisition contaminated by uncorrelated Gaussian noise for 41 stations along the 40-km survey line, run over discretizations A and B. The results of seven macro-iterations of a Hybrid D-Wave workflows such as Kerberos (top panel) and Hybrid (bottom panel) with optimal lambda value are shown for discretizations A, colored in blue. The real shape of the target is overlaid in orange. Matching voxels are highlighted in purple.

seems promising with respect to conventional solvers such as simulated annealing and hybrid default D-Wave workflows. The results can be considered relevant compared to those obtained in the ref. [4].

The proposed method has the potential of providing a fast way of computing inverted images from gravity data, using all the information we have to reduce the space of admissible solutions to this ill-posed problem.

As far as computational resources are concerned, finding the fair terms for the comparison of this heuristics with the genetic optimization algorithm-based binary inversion by Krahenbuhl[4] is a complex task. In the reference work, as the minimization of the cost function was carried out via a genetic optimization algorithm, a reference value denoting the computational cost might be the number of generations needed to obtain comparable results. The main parameter that denotes the potential of an inversion implementation on quantum computers is the number of iterations performed for each model. Once the boundary quadratic model is built, all gradient iterations needed to find the optimal Lagrange parameter in Equation (15) can be gathered in a customized hybrid workflow as in ref. [26]. Hence, the relevant parameter that defines the computational cost is the number of macro-iterations performed in the inversion stages, compared to the number of generations required in the genetic algorithm illustrated in ref. [4]. In **Table 2**, we gather the numbers that are relevant to the comparison. Moreover, further reduction of the number of macro-iterations is foreseeable as far as the progress in quantum annealers will allow an accurate representation of complete graphs with quadratic terms of different magnitudes.

As both the result quality and the number of iterations needed to get a result are affected by a restricted representation of the complete graph associated with the inversion binary quadratic model, we are far from claiming any quantum advantage of our implementation for the case under study.

Table 2. Number of macro-iterations of the proposed heuristics on the quantum annealer (QA iterations) compared to the number of macro iterations of the same algorithm running on conventional simulated annealing (SA iterations) and to the number of generations of the genetic optimization algorithm (CC iterations) employed by ref. [4] on conventional hardware, for the numerical experiments presented in Sections 3.1 and 3.2. For benchmark 3.2 in the QA case we consider the hybrid approach with one iteration purely QA and one SA.

Numerical example	QA iterations	SA iterations	CC iterations
3.1	6	6	300
3.2	2	6	500

Aside from conventional computational costs due to binary quadratic model coefficient evaluation at each macro-iteration and to the solution of the direct problem to evaluate the predicted gravity response for each iteration of the loop, we gather the quantum processing computational costs for different spatial discretizations for the same numerical experiment in **Table 3**.

We considered different spatial discretizations for the numerical experiment with constant density contrast in Section 3.1. The numerical experiments were run utilizing a standard sampler through a cutoff composer with a threshold set to 0.75 over 1000 shots. Basically, if the computed problem fits on the QPU, the computational cost of the single quantum annealing descent is constant. Repeating the numerical experiments for different annealing time values in the set $\{1, 2, 5, 10, \text{and } 20 \, \mu s\}$, we obtained constant QPU access values with respect to the computational grid, ranging from 160 to 179 ms. As far as the inversion image quality is concerned, no relevant improvements are noticeable with a long-lasting annealing time.

In order to compare the performances with a classic solver, we conducted the same series of numerical experiments for the same heuristics choosing the conventional simulated annealing sampler included in the D-Wave distribution. We obtain results that are qualitatively similar to those evaluated with the cutoff composer in the QPU, keeping into account that for such a meta-heuristic algorithm as well, the solution is intrinsically

Table 3. Scalability of the method: Comparison of annealing computational time per micro-iteration. The first column displays the discretization labels as in Table 1, the second column gathers the number of active qubits after the imposition of the constraint that sets binary values to zero. In the three following column QPU access time values, intended as in ref. [31], are listed for Advantage2 prototype 1.1 (A2), Advantage 5.1 (A5.1), and D2000W devices, setting the annealing time value to 10 μs. Postprocessing (PP) times are indicated in the fifth column for conventional postprocessing of the solution with a greedy gradient solver. Simulated annealing times (mean value for micro-iteration run) appear in the sixth column. All computational times on conventional hardware are referred to a Intel(R) Xeon(R) CPU E5-2683 v3 2.00GHz processor.

Mesh label	Active qubits	QPU A2 [ms]	QPU A5.1 [ms]	QPU D2000W [ms]	PP time [s]	SA time [s]
A	825	65	173	400	0.2	1.5
B	1420	65	173	400	0.7	4.5
C	3232	65	173	400	1.7	22

**ADVANCED
SCIENCE NEWS**

www.advancedsciencenews.com

**ADVANCED
QUANTUM
TECHNOLOGIES**

www.advquantumtech.com

probabilistic. As far as computational time for the simulated annealing is concerned, we are interested to see how it scales with respect to the number of qubits of the three different grids defined in Table 1. The results are listed in Table 3, considering three different QPUs (Advantage2 prototype 1.1, Advantage 5.1, and DW2000v6) characterized by different embedding layouts (zephyr, pegasus, and chimera). As far as the computational time on conventional resources, we provide the mean value of the micro-iteration computational time. Table 3 suggests that the average time complexity of simulated annealing might be polynomial, in contrast to the behavior we observed on QPUs. This is in agreement with Sasaki[30] that indicates for simulated annealing an average time complexity of $O(n^4)$ for a typical graph with n nodes.

Hence, an investigation on how the computational time scales with the number of qubits shows computational advantage using the existing quantum methods to solve an inversion problem.

Further work will be done to provide a more efficient implementation of the inner micro-iteration loop we evaluate to identify the optimal Lagrange value for a single binary quadratic model, that is, absorbing the whole set of instructions on a customized annealer workflow.

5. Conclusions

In our work, we provide a quantum-enhanced implementation of a method inspired by the binary inversion method proposed by Krahembuhl and Li.[4]

Our heuristics were able to reconstruct the discontinuity anomaly from realistic 2D gravity datasets. The results we obtain provide a good sharp subsurface model from surface data, whose quality is comparable to the reference work.[4] Despite the limitations arising when mapping a complete problem graph on existing quantum hardware do not allow to neatly outperform classical results, the proposed heuristics makes the constrained gravity data inversion a usable technique that reconstructs the subsurface model in less than ten macro-iterations, compared to the hundreds of generations required by genetic algorithms in ref. [4]. Moreover, the hybrid quantum solution we provide for non-convex benchmarks in the presence of annihilators seems promising with respect to conventional solvers such as simulated annealing and hybrid default D-wave workflows. Furthermore, as far as the part of the computation that resides in the QPU is concerned, the computational cost of the single quantum annealing descent is constant with respect to the number of degrees of freedom of the subsurface model. The results make the generalization of the present heuristics to 3D cases and non-trivial variable density contrasts closer. Even if a quantum advantage for the inversion application on the currently available hardware has not been demonstrated, thanks to the improvements in quantum annealing methods and hardware, these fast inversion methods might become a killer application for QPUs, thus creating a valuable alternative to quite expensive iterative methods on conventional hardware. The implemented method is likely to reveal its full potential on forthcoming quantum annealing devices that will provide improved embedding capabilities for complete graphs, outperforming existing techniques.

Conflict of Interest

The authors declare no conflict of interest.

Data Availability Statement

Research data are not shared.

[1] J. Hadamard, *Lectures on Cauchy's Problem in Linear Partial Differential Equations*, Yale University Press, New Haven **1923**.

[2] Y. Li, D. W. Oldenburg, *Geophysics* **1998**, *63*, 109.

[3] H. Cai, B. Xiong, Y. Zhu, in *Gravity* (Ed: T. Zouaghi), IntechOpen, Rijeka **2018**, Ch. 2.

[4] R. A. Krahenbuhl, Y. Li, *Geophys. J. Int.* **2006**, *167*, 543.

[5] N. Ye, F. Roosta-Khorasani, T. Cui, in *2017 MATRIX Annals* (Eds: D. R. Wood, J. de Gier, C. E. Praeger, T. Tao), Springer, Cham **2019**, pp. 121–140.

[6] H. Wang, L. Wu, *Sci. Rep.* **2016**, *6*, 22307.

[7] P. Date, D. Arthur, L. Pusey-Nazzaro, *Sci. Rep.* **2021**, *11*, 10029.

[8] C. Baldassi, R. Zecchina, *Proc. Natl. Acad. Sci. U. S. A.* **2018**, *115*, 1457.

[9] E. Farhi, J. Goldstone, S. Gutmann, M. Sipser, *arXiv:quant-ph/0001106*, **2000**.

[10] A. Ajagekar, F. You, *Comput. Chem. Eng.* **2020**, *143*, 107119.

[11] D. Herman, C. Googin, X. Liu, A. Galda, I. Safro, Y. Sun, M. Pistoia, Y. Alexeev, *arXiv:2201.02773*, **2022**.

[12] L. Rocutto, C. Destri, E. Prati, *Adv. Quantum Technol.* **2021**, *4*, 2000133.

[13] L. Rocutto, E. Prati, *Int. J. Quantum Inf.* **2021**, *19*, 2141003.

[14] F. Aminzadeh, J. Brac, T. Kunz, *SEG/EAGE 3-D Salt and Overthrust Models*, SEG/EAGE 3-D Modeling Series, No. 1, Society of Exploration Geophysicists, Tulsa **1997**.

[15] S. Kirkpatrick, C. Gelatt, M. Vecchi, *Science* **1983**, *220*, 671.

[16] A. Tikhonov, V. Arsenin, *Solutions of Ill-posed Problems*, V.H. Winston & Sons, Washington DC **1977**.

[17] K. Nozaki, *Earth Planets Space* **2006**, *58*, 287.

[18] R. J. Blakely, *Potential Theory in Gravity and Magnetic Applications*, Cambridge University Press, Cambridge, NY **1995**.

[19] D-Wave Systems Inc., Problem-Solving Handbook, Version: 9-1171B-E, https://docs.dwavesys.com/docs/latest/doc_handbook.html (accessed: June 2021).

[20] D-Wave Systems Inc., Solver Properties and Parameters, https://docs.dwavesys.com/docs/latest/doc_solver_ref.html (accessed: December 2021).

[21] F. Glover, G. Kochenberger, Y. Henning, R. Hennig, Y. Du, *Ann. Oper. Res.* **2022**, *314*, 141.

**ADVANCED
SCIENCE NEWS**

www.advancedsciencenews.com

**ADVANCED
QUANTUM
TECHNOLOGIES**

www.advquantumtech.com

[22] P. Date, R. Patton, C. Schuman, T. Potok, *Quantum Inf. Process.* **2019**, *18*, 117.

[23] D. Oldenburg, Y. Li, in *Near-Surface Geophysics* (Ed: D. K. Butler), SEG Book Series, Society of Exploration Geophysicists, Tulsa **2005**, Ch. 5.

[24] M. F. Hutchinson, F. Hoog, *Numer. Math.* **1985**, *47*, 99.

[25] J. W. Tukey, in *Spectral Analysis of Time Series* (Ed: B. Harris), Wiley, New York **1967**, pp. 25–46.

[26] D-Wave Systems Inc., D-Wave Hybrid, Release 0.6.5, https://docs.ocean.dwavesys.com/_/downloads/hybrid/en/latest/pdf/ (accessed: January 2022).

[27] D-Wave Systems Inc., *D-Wave Ocean Simulated Annealing Sampler*, https://docs.ocean.dwavesys.com/en/stable/docs_neal/reference/sampler.html (accessed: August 2023).

[28] Y. Koshka, M. A. Novotny, *IEEE J. Sel. Areas Commun.* **2020**, *1*, 515.

[29] R. L. Parker, *Annu. Rev. Earth Planet. Sci.* **1977**, *5*, 35.

[30] G. H. Sasaki, *Ph.D. Thesis*, University of Illinois Urbana-Champaign **1987**.

[31] D-Wave Systems Inc., QPU Solver Datasheet. User Manual, Version: 09-1109B-E, https://docs.dwavesys.com/docs/latest/doc_qpu.html (accessed: November 2021).